nature nanotechnology

ARTICLES

https://doi.org/10.1038/s41565-018-0188-x

High Purcell factor generation of indistinguishable on-chip single photons

Feng Liu[1,4,6], Alistair J. Brash[1,6*], John O'Hara[1,6], Luis M. P. P. Martins[1], Catherine L. Phillips[1], Rikki J. Coles[1], Benjamin Royall[1], Edmund Clarke[2], Christopher Bentham[1], Nikola Prtljaga[1,5], Igor E. Itskevich[3], Luke R. Wilson[1], Maurice S. Skolnick[1] and A. Mark Fox[1]

On-chip single-photon sources are key components for integrated photonic quantum technologies. Semiconductor quantum dots can exhibit near-ideal single-photon emission, but this can be significantly degraded in on-chip geometries owing to nearby etched surfaces. A long-proposed solution to improve the indistinguishablility is to use the Purcell effect to reduce the radiative lifetime. However, until now only modest Purcell enhancements have been observed. Here we use pulsed resonant excitation to eliminate slow relaxation paths, revealing a highly Purcell-shortened radiative lifetime (22.7 ps) in a waveguide-coupled quantum dot–photonic crystal cavity system. This leads to near-lifetime-limited single-photon emission that retains high indistinguishablility (93.9%) on a timescale in which 20 photons may be emitted. Nearly background-free pulsed resonance fluorescence is achieved under π-pulse excitation, enabling demonstration of an on-chip, on-demand single-photon source with very high potential repetition rates.

Integrated quantum photonics has made great progress in recent years, with quantum functionality demonstrated in boson sampling and interferometer sensitivity applications[1]. However, scaling beyond the few-photon level is presently limited by large losses from the use of off-chip single-photon sources (SPSs), with the current state of the art operating at the 3–5 photon level[2–5]. Though SPSs have been realized on-chip using four-wave mixing[6], the very low efficiency imposes significant limitations. A solution to this issue would be to integrate deterministic SPSs on-chip[7–12]. Among the possible candidates for such sources, semiconductor quantum dots (QDs) have been shown to offer nearly ideal performance when emitting into free space[13–16]. In particular, photon indistinguishabilities of 92.1% and ~98% have been demonstrated with microsecond[17] and nanosecond[15,16] photon separation times, respectively.

The photon indistinguishability on short timescales is determined by $T_2/(2T_1)$, where T_1 is the emitter lifetime and T_2 is the coherence time described by $1/T_2 = 1/(2T_1) + 1/T_2^*$. T_2^* is defined as the pure dephasing time characterizing the homogeneous (Lorentzian) broadening beyond the natural linewidth. The indistinguishability on long timescales can be further reduced by inhomogeneous (Gaussian) broadening on a timescale much longer than T_1, for example, spectral wandering caused by a fluctuating charge environment. The integration of QD sources into on-chip geometries has been observed to significantly reduce photon indistinguishability due to increased charge fluctuations from the nearby etched surfaces[9,18–20]. A long-proposed[18,21] approach to overcoming these effects is to use the Purcell effect to enhance the radiative emission rate $1/T_1$ (refs [22,23]). In theory, strong Purcell enhancement could be obtained by fabricating QDs in cavities with a high Q-factor and small mode volume—such as photonic crystal cavities (PhCCs). However, previously directly measured T_1 have reached only ~150 ps, corresponding to a Purcell factor (F_P) of only ~10 (refs [23–27]), over an order of magnitude smaller than the maximum theoretical value. Most studies attribute the large discrepancy to poor spatial overlap between the QD and the cavity mode[28] or insufficient detector time resolution[25]. Shorter $T_1 \sim 50$ ps indirectly inferred from multiple-parameter fitting was also reported[25,29].

In this Article we show unambiguously that larger Purcell enhancements can be achieved by applying pulsed resonant excitation to an InGaAs QD in a waveguide-coupled PhCC. The strongly Purcell-shortened T_1 (22.7 ± 0.9 ps) leads to lifetime-limited coherence ($T_2/(2T_1) \approx 1$) and high photon indistinguishability on a timescale in which the source can potentially emit 20 photons. The record-short T_1 is directly measured using a new double π-pulse resonance fluorescence (DPRF) technique and independently verified by resonant Rayleigh scattering (RRS) measurements. Combining very low power π-pulse excitation and on-chip guiding, we achieve nearly background-free pulsed resonance fluorescence in an on-chip geometry, enabling demonstration of an on-chip electrically-tunable SPS meeting three key requirements for quantum information processing: on-demand operation, high single-photon purity (97.4%) and high indistinguishability (93.9%). Particularly, the short T_1 implies high achievable source repetition rates of ~10 GHz, crucial for realistic on-chip demultiplexing of the photons.

Sample design and characterization

The Purcell factor is determined by the properties of the cavity and the overlap between the QD and the cavity mode, and is given by[23]:

$$F_P = \frac{T_1'}{T_1} = \frac{3Q}{4\pi^2 V_m} \frac{(2\kappa)^2}{4(\omega - \omega_{cav})^2 + (2\kappa)^2} \frac{|\boldsymbol{\mu} \cdot \mathbf{E}(\mathbf{r}_0)|^2}{|\boldsymbol{\mu}|^2 |\mathbf{E}_{max}|^2} \quad (1)$$

[1]Department of Physics and Astronomy, University of Sheffield, Sheffield, UK. [2]EPSRC National Epitaxy Facility, Department of Electronic and Electrical Engineering, University of Sheffield, Sheffield, UK. [3]School of Engineering and Computer Science, University of Hull, Hull, UK. [4]Present address: JARA-Institute for Quantum Information, RWTH Aachen University, Aachen, Germany. [5]Present address: Gooch & Housego (Torquay), Torquay, UK. [6]These authors contributed equally: Feng Liu, Alistair J. Brash, John O'Hara. *e-mail: a.brash@sheffield.ac.uk

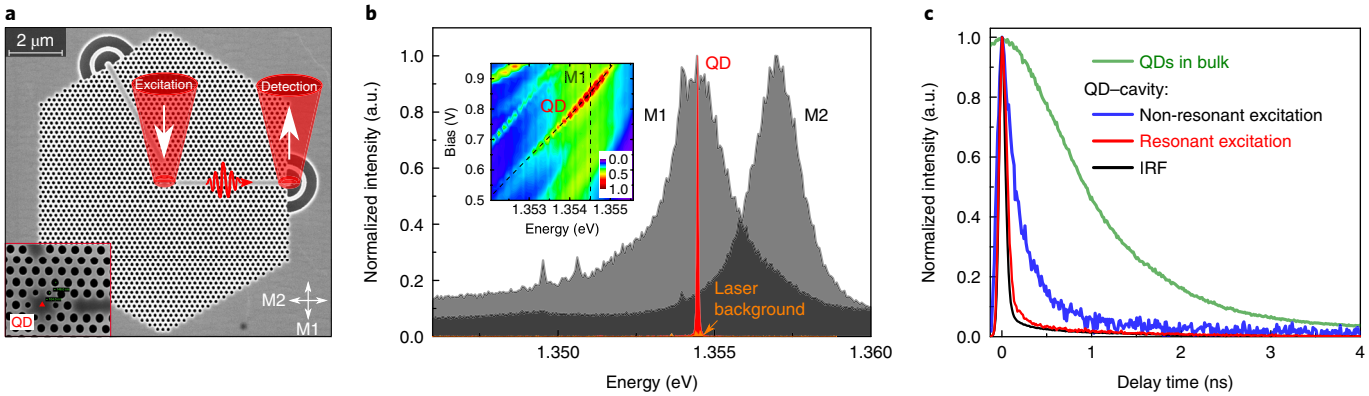

Fig. 1 | Details of the waveguide-coupled QD-H1 PhCC system. a, Scanning electron microscope image of the device. When operated as an on-chip SPS (see Fig. 4), the QD is excited via the cavity and the single-photon emission is collected from the out-coupler. All other measurements are performed by collecting directly from the cavity to maximize the intensity of the RF signal. Inset: a close-up of the cavity. **b**, Grey: high-power PL spectra under non-resonant excitation ($\lambda_{exc}=802$ nm). Two orthogonally linearly polarized modes (M1 and M2) are observed when detecting with horizontal (H) and vertical (V) polarization, respectively. Red: single QD emission measured with resonant π-pulse excitation. The laser background (orange) is measured by detuning the QD from the laser and is more than 20 times weaker. Inset: low-power PL as a function of the bias and energy under non-resonant excitation. The neutral exciton (X) is electrically tunable by 5.2 meV from bias = 0.2 to 0.93 V (oblique dashed line). Maximum Purcell enhancement of the QD emission is observed around 0.83 V, where the QD is resonant with the M1 mode (vertical dashed line). **c**, Normalized PL decay of the QD ensemble in bulk measured with non-resonant excitation (green) and that of the QD in cavity measured under non-resonant (blue) and resonant (red) excitation at bias = 0.83 V. Black: instrument response function (FWHM = 60 ps).

where T_1' is the exciton radiative lifetime in the absence of a cavity; Q is the quality factor of the cavity, and V_m its mode volume in cubic wavelengths $(\lambda/n)^3$; ω, ω_{cav} and 2κ denote the angular frequency of the exciton transition, the cavity resonance and the full-width at half-maximum (FWHM) of the cavity mode; and $\boldsymbol{\mu}$, $\mathbf{E}(\mathbf{r}_0)$ and $\mathbf{E}_{max}$ represent the transition dipole moment, the electric field at the QD position and the maximum electric field.

To obtain strong Purcell enhancement across a large QD tuning range, we integrate the QD into an H1 PhCC with small mode volume ($V_m \approx 0.63\ (\lambda/n)^3$) and moderate Q (see Fig. 1). The cavity has two orthogonally linearly polarized fundamental modes (M1 ($Q=540$) and M2 ($Q=765$)) (shaded grey lines in Fig. 1b). The upper theoretical limit of the F_P value is 65 for the M1 mode (see Supplementary Information Section 1). To extract the photons from the cavity and guide them on-chip, we integrate two W1 photonic crystal waveguides. Each is coupled to one cavity mode[30,31] and terminated with an out-coupler. Integrating the photonic crystal structure into a p-i-n diode (see Supplementary Information Section 2) allows tuning of the neutral exciton (see Supplementary Information Section 3) by ~5 meV via the quantum-confined Stark effect (see inset in Fig. 1b). Clear enhancement of the photoluminescence (PL) intensity is observed when the neutral exciton X is resonant with the M1 cavity mode.

To investigate the Purcell-shortened T_1, we first perform time-resolved measurements using a fast single-photon avalanche diode (SPAD). The PL decay time (262 ± 3 ps, blue line in Fig. 1c) measured with the QD resonant with the M1 cavity mode under non-resonant excitation ($\lambda_{exc}=802$ nm) is shortened by a factor of approximately four compared with that of ensemble QDs ($T_1'=971\pm15$ ps), a mean value obtained using four different locations outside the photonic crystal (one is shown, green line). The distribution of the QD ensemble peaks at around 1.353 eV, very close to the emission energy (1.354 eV) of the QD on which we focus. Under resonant excitation, the PL decay time of the QD in the cavity is further shortened by at least a factor of six (to 46.2 ± 1.2 ps without deconvolution, red line), a value limited by the instrument response function (IRF) of the SPAD (FWHM = 60 ps, black line). We attribute the difference of the PL decay time under resonant and non-resonant excitation to a long carrier relaxation time from higher-energy states to the lowest exciton state[32–34], supported by simulations (see Supplementary Information Section 4A). The slow carrier relaxation masks the real F_P value and limits the indistinguishability of QD SPSs[21]. This observation implies that in the case of strong Purcell enhancement, T_1 can be accurately measured only when the exciton is populated much faster than the radiative recombination rate, in this case by resonant excitation. In addition, since in our sample T_1 cannot be clearly resolved by the fastest SPADs available, a technique with higher time resolution is required.

Double π-pulse resonance fluorescence measurement

To measure T_1 accurately, we develop a DPRF technique with a time resolution ultimately limited by the laser pulse duration ($T_P=13$ ps) (see details in Methods and Supplementary Information Section 4B), making it possible to measure a T_1 much shorter than the time resolution of SPADs. The principle of the DPRF technique is illustrated in Fig. 2a. The QD can be treated as a two-level system consisting of a crystal ground state (CGS) $|0\rangle$ and an exciton state $|X\rangle$ with a total population of 1. At $t=0$, a laser pulse with a pulse area $\Theta=\pi$ coherently drives the QD to $|X\rangle$, creating an X population close to 1. The area Θ is calibrated by performing a Rabi oscillation measurement[35] (see Fig. 2b). Before the second pulse arrives, the exciton population radiatively decays to $C_X=e^{-\Delta t/T_1}$ via spontaneous emission (SE), where Δt is the inter-pulse delay. The probability of photon emission up to time Δt is equal to $(1-C_X)$. At $t=\Delta t$, the second π-pulse exchanges the populations of $|0\rangle$ and $|X\rangle$. The exciton population is now $(1-C_X)$ which subsequently decays to the ground state. The total resonance fluorescence (RF) intensity (I_{RF}) measured by the DPRF technique is therefore described by:

$$I_{RF}\propto 2(1-C_X)=2(1-e^{-\Delta t/T_1}) \quad (2)$$

Figure 2c shows the result of the DPRF measurement at QD–cavity detuning $\Delta E=0$. I_{RF} recovers with Δt on the timescale of the exciton radiative lifetime. Fitting the curve with equation (2) yields a record-low T_1 of 22.7 ± 0.9 ps, corresponding to a very high Purcell factor for a QD–nanocavity system of 43 ± 2 (for $T_1'=971\pm15$ ps). The RF signal saturates at a pulse separation of around 100 ps in Fig. 2c, opening a route to repetition rates as high as 10 GHz. Below

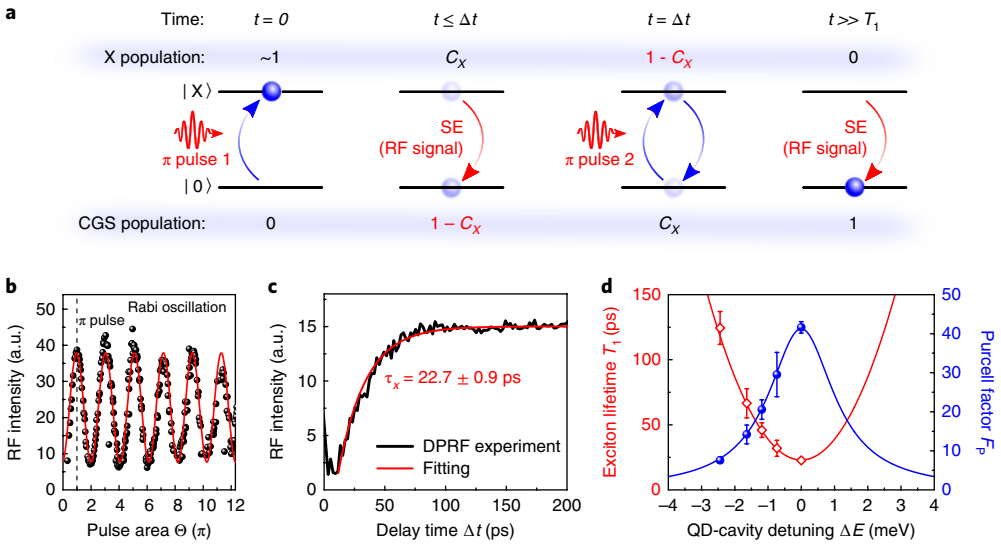

Fig. 2 | The DPRF technique. a, The principle of the measurement. SE: spontaneous emission. **b**, RF intensity of the QD as a function of the pulse area Θ of a single pulse, showing Rabi oscillations (red line shows sine fit). $\Theta = \mu/\hbar \int_{-\infty}^{+\infty} E(t)dt$, where μ and $E(t)$ denote the transition dipole moment and the laser field. **c**, DPRF measurement: the RF intensity as a function of the time delay Δt between the π-pulses. Fitting (red) with a single exponential function gives an exciton radiative lifetime of 22.7 ± 0.9 ps. **d**, The dependence of T_1 (red diamonds) and F_P (blue dots) on the QD–cavity detuning $\Delta E = E_X - E_c$, where E_X and E_c are the energies of the exciton and cavity resonances, respectively. Error bars derive from the uncertainty in the exponential fits from which T_1 and T_1' are extracted. Solid lines: simulations using equation (1).

saturation, there is a significant probability of emitting zero rather than the desired two photons (see Supplementary Information Section 4B), defining an upper bound on the excitation repetition rate for SPS applications. Unlike for slower sources, on-chip delays of ~100 ps can readily be realized[36], paving the way for on-chip time demultiplexing, which is an important requirement for integrated photonic circuits.

Detuning the QD away from the cavity resonance increases (decreases) T_1 (F_P) (see Fig. 2d). This trend is well reproduced by equation (1) with the cavity linewidth (2.5 meV) extracted from the PL spectra (see Fig. 1b) and a spatial overlap of ~81%, further showing that the short T_1 results from a large Purcell enhancement.

Our findings demonstrate two advantages of low-Q cavities for on-chip SPSs. First, though the QD-cavity coupling strength ($\hbar g$) estimated from the F_P value is as large as 135 μeV (see Supplementary Information Section 1), the low Q ensures that the system remains in the weak-coupling regime, as required for efficient coherent single-photon emission. Second, a very short T_1 (≤30 ps) may be maintained within a large tuning range (1.4 meV), giving an electrically-tunable source of on-chip single photons.

Resonant Rayleigh scattering

To further verify the short T_1 and probe the pure dephasing of the emitter, we switch to resonant continuous-wave (CW) excitation. The transition is driven at the Rabi frequency Ω_R, and the exciton population and coherence have damping constants $\gamma_1 = 1/T_1$ and $\gamma_2 = 1/T_2$, respectively. In the weak-driving limit, where $(\Omega_R)^2 \ll \gamma_1\gamma_2$, the scattered field is dominated by RRS provided $T_2 > T_1$ (refs [37–39]). These coherently scattered photons are antibunched but retain the linewidth (and thus coherence) of the laser. The ratio of the RRS intensity to the total (RRS + SE) intensity is given by[39]:

$$\frac{I_{RRS}}{I_{total}} = \frac{T_2}{2T_1} \frac{1}{1 + (\Omega_R)^2/(\gamma_1\gamma_2)} \quad (3)$$

Equation (3) suggests that reducing T_1 through a strong Purcell effect will lead to a high fraction of RRS. To demonstrate this, high-resolution spectroscopy is performed using a scanning Fabry–Pérot interferometer (FPI) (see Methods). At high driving strengths (Fig. 3, right-hand inset), the spectrum consists of a sub-microelectronvolt component from RRS with a broad contribution from SE which vanishes at lower driving strengths (left-hand inset). By fitting the spectra, the ratio I_{RRS}/I_{total} may be evaluated as a function of Ω_R.

A fit using equation (3) (see Supplementary Information Section 5A) is included in Fig. 3 as an orange line and gives $T_1 = 24.6 \pm 1.6$ ps and $T_2 = 49.2 \pm 5.4$ ps, providing an independent measure of the short radiative lifetime, and showing that the strong Purcell enhancement successfully eliminates the effect of pure dephasing, resulting in close to lifetime-limited coherence ($T_2/(2T_1) \approx 1$).

On-chip on-demand single-photon source

To generate strings of single photons on-demand we now study our device under resonant π-pulse excitation. QDs driven by π-pulses have proven to be an excellent source of single photons owing to their high purity, indistinguishability and on-demand operation[14–16]. Such performance would be highly desirable for an on-chip SPS. However, to date all QD SPSs driven by resonant π-pulses have emitted into free space. By exciting on the cavity and collecting from the waveguide (see Fig. 1a), we achieve nearly background-free pulsed RF (see red and orange lines in Fig. 1b), realizing a resonantly-driven on-chip on-demand SPS. Compared with QDs in bulk or relatively large nanostructures, it is significantly more experimentally demanding to realize background-free pulsed RF in photonic crystal structures because the patterned surface scatters the polarization of the reflected laser.

To characterize the purity of the source, a Hanbury Brown and Twiss (HBT) correlation measurement is performed under resonant π-pulse excitation. The results are shown in Fig. 4a, where the area of the grey time-zero peak for a 13 ps pulse gives a purity $(1-g^{(2)}_{HBT}(0))$ of 86.6 ± 0.3% at an unfiltered signal-to-background ratio (SBR) of approxiamtely 20:1. Simulations (inset to Fig. 4a, see also Supplementary Information Section 4C) show that the measured single-photon purity is limited primarily by multiple emissions originating from re-excitation of the source by a pulse that is

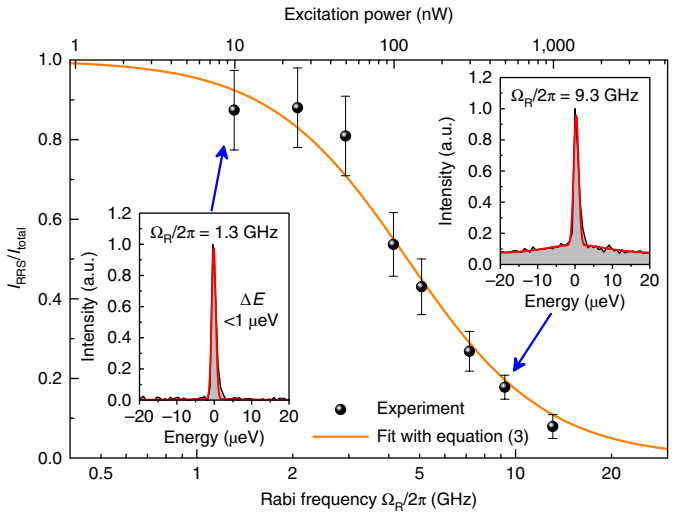

Fig. 3 | Plot of the ratio of the coherently scattered laser photons (I_{RRS}) to the total scatter ($I_{total} = I_{RRS} + I_{SE}$) as a function of Rabi frequency and CW excitation power. Error bars represent the uncertainty in the fits to the FPI spectra. Orange line: fit using equation (3). Insets: high-resolution spectra of the QD emission under weak (left) and strong (right) CW resonant driving, measured with a FPI. Red lines: fits of the RRS and SE (see Supplementary Information Section 5A).

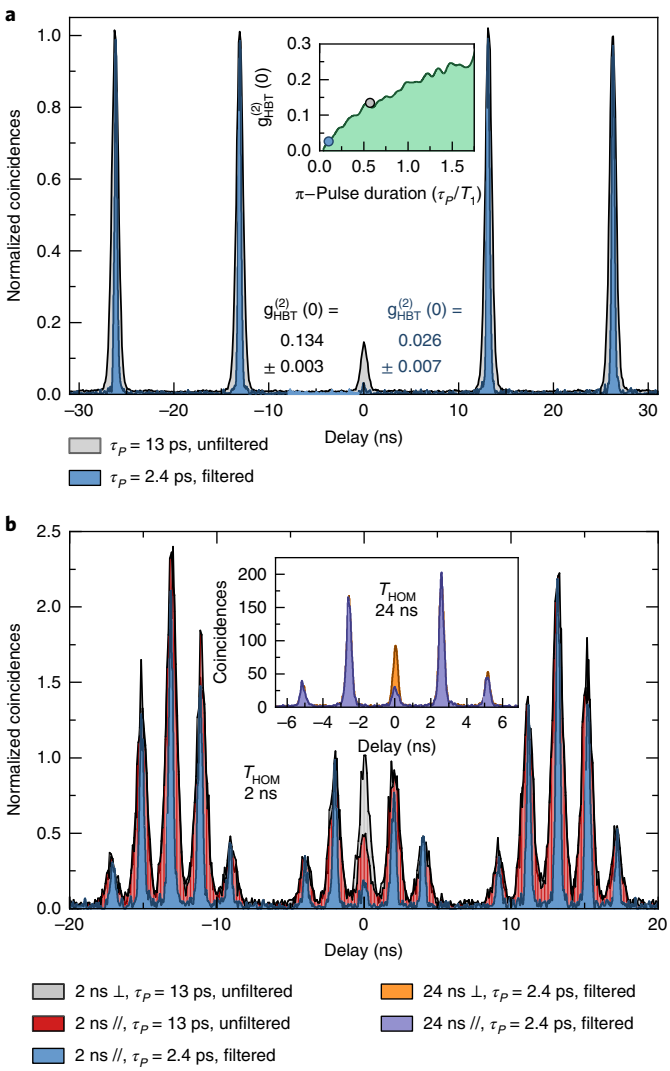

Fig. 4 | Second-order correlation measurements of the waveguide-coupled QD emission under resonant π-pulse excitation. a, HBT measurement of single-photon purity ($1-g^{(2)}_{HBT}(0)$) using 13 ps (grey) or 2.4 ps (blue) pulses. Inset: simulation of $g^{(2)}_{HBT}(0)$ as a function of π-pulse duration T_p relative to T_1, where coloured circles correspond to experimental data (see Supplementary Information Section 4C). **b**, Hong–Ou–Mandel measurement of interference visibility for photons emitted 2 ns apart. The red and grey data show coincidence counts for co- (||) and cross-polarization (⊥) of the two interferometer arms, respectively, when the source is driven by 13 ps pulses. The blue data shows the co-polarized case for 2.4 ps pulses. Inset: HOM measurement for photons emitted 24 ns apart. Note that the peak area pattern differs from the main figure as $(1/T_{HOM}) < 76.2$ MHz (the laser repetition rate), thus the peaks adjacent to zero delay now originate from different pulses. See Methods and Supplementary Information Section 6 for further details.

relatively long compared to T_1. To test this hypothesis and suppress multiple emissions during the pulse, the measurement is repeated with a 2.4 ps pulse (blue data in Fig. 4a). Owing to the intrinsic birefringence of the optical set-up, a 96 μeV grating filter is required to eliminate residual scatter of the spectrally broad pulse from the sample surface, resulting in an SBR ≈ 50:1. We emphasize that such filtering is required only because of the combination of out-of-plane collection geometry and relatively short (5 μm) waveguide length; this would not be required for on-chip experiments. In agreement with simulations, the measured purity increases to 97.4 ± 0.7% with the shorter pulse. For 13 ps pulses, the filtered and unfiltered purities are very similar, indicating that the purity is improved by the reduced pulse duration rather than the filtering.

Using a fibre Mach–Zehnder interferometer (see Supplementary Information Section 6), Hong–Ou–Mandel (HOM) interferometry is performed to determine the indistinguishability of photons emitted from the source (Fig. 4b). When the photon separation (T_{HOM}) is 2 ns and a 13 ps pulse is used without filtering, the visibility (V) is 60.1 ± 3.2% after correcting for the interferometer properties (see Supplementary Information Section 6). If $g^{(2)}_{HBT}(0)$ is also corrected for, this rises to $V = 79.7 \pm 5.9\%$. By again reducing the pulse duration to 2.4 ps, the visibility increases to 89.4 ± 2.5% (93.9 ± 3.3%) without (with) correction for $g^{(2)}_{HBT}(0)$, implying a $T_2/(2T_1)$ ratio close to unity, in agreement with the RRS measurements.

The improved visibility with the 2.4 ps pulse is mainly due to the previously discussed reduction of multiple emission events, though the spectral filter also acts to remove a significant amount of the phonon sideband. Recent studies have indicated that the unfiltered visibility of single photons from non-Purcell-enhanced InGaAs QDs at 4.2 K is limited to around 80% by incoherent phonon sideband emission[40]. This can be improved without the losses of filtering by placing the QD in a resonant high-Q cavity[40]. In the device studied here, though there is a strong Purcell enhancement, the relatively low Q means that the cavity filtering effect is weaker, introducing a theoretical upper bound on the unfiltered visibility of ~90%, rising to ~99% if the grating filter is added[40]. A separation of $T_{HOM} = 2$ ns would correspond to 20 emission cycles of the source (if driven at 10 GHz), adequate to significantly exceed the complexity of any boson sampling experiments to date[2–5].

To explore any potential degradation of the visibility at longer timescales, the separation is extended to $T_{HOM} = 24$ ns (potentially 240 emission cycles) (see inset to Fig. 4b). This results in a visibility of 75.3 ± 2.0% (79.9 ± 3.4%) without (with) correction for $g^{(2)}_{HBT}(0)$, a decrease of 14% compared to $T_{HOM} = 2$ ns. As this timescale is much greater than T_1, the decline in visibility is attributed to spectral wandering due to a charge environment fluctuating on a timescale of tens of nanoseconds. Previous studies of QD microlens

structures (which also include etched surfaces relatively close to the QD) exhibited a significantly larger wandering-induced visibility decay of ~40% on a comparable timescale (12.5 ns)[41]. The critical advantage of the device studied here is that the very short T_1 broadens the natural linewidth by a factor of F_P, minimizing the visibility degradation while also allowing photons to be extracted much faster than spectral wandering timescales.

Discussion

For on-chip single-photon sources, reduced photon indistinguishability through environmental interactions has been a major concern. This is especially true for waveguide-coupled sources, which by necessity are situated near surfaces[42]. In this Article, the effect of pure dephasing on the waveguide-coupled QD emission has been made negligible through use of the Purcell effect and resonant excitation, as is shown by the high RRS fraction and high HOM visibility for short pulse separations.

Another potential issue, as the comparison of different HOM photon separations indicates[17,41,43], is wandering due to a fluctuating charge environment. This is also mitigated by the Purcell enhancement, since the ratio between the lifetime-limited linewidth of the QD emission and the width of the wandering is reduced by a factor of $F_P \sim 40$. We note that this is a first-generation device, and further improvement of the indistinguishability at long photon separation times could potentially be achieved by reducing the charge fluctuations via surface passivation[19] or by optimizing the sample growth and diode structure[44]. We also note that keeping all other parameters constant, increasing Q to 2,500 (the onset of strong coupling) by optimizing fabrication would give $F_P \sim 200$ (see Supplementary Information Section 1), further suppressing the influence of spectral wandering, while also improving the theoretical unfiltered visibility to ~97% by reducing the phonon sideband content of the emission[40]. In off-chip experiments driven by QD SPSs, visibilities of ~65% have been sufficient to demonstrate boson sampling[5,43], with 94% being the current state of the art[4]. This confirms the feasibility of harnessing our source architecture to perform such quantum optics experiments on a single chip.

Besides indistinguishability, the count rate measured by a detector is another important figure-of-merit. Using experimentally demonstrated parameters for the GaAs platform (see Supplementary Information Section 7), the count rate is predicted to be ~4 MHz for a SPS driven at 76.2 MHz and connected to a superconducting nanowire single-photon detector (SNSPD) via a 100 μm photonic crystal waveguide. This is comparable to the highest count rate (9 MHz) of micropillar-based off-chip SPSs[4]. Thanks to the large Purcell enhancement, the maximum count rate for our source can potentially reach ~540 MHz when driven with a pulse repetition rate of 10 GHz. Beyond this, optimizing the cavity–waveguide coupling[31], improving the SNSPD efficiency[45] and increasing the cavity Q presents a clear path to GHz on-chip count rates, showing the great potential of this approach for integrated quantum photonics.

Conclusions

In this Article we unambiguously reveal a strongly Purcell-shortened exciton radiative lifetime of only 22.7 ps in a photonic crystal cavity using pulsed resonant excitation. This is directly measured by a novel high-time-resolution DPRF technique. Electrically tunable on-demand single photons from the cavity are efficiently channelled into a waveguide with minimal laser background, allowing the device to operate as an on-chip SPS. The short radiative lifetime (T_1) opens the way to source repetition rates ~10 GHz which are compatible with on-chip delays for time demultiplexing[36] and could lead to detected on-chip count-rates of ~540 MHz using experimentally demonstrated parameters.

Additionally, the small T_1 eliminates the effect of pure dephasing and suppresses the influence of spectral wandering. This leads to lifetime-limited emitter coherence and high single-photon purity (97.4%). Indistinguishabilities of >90% are measured on a timescale of 2 ns (potentially 20 photon emission events when driven at 10 GHz) or ~80% for 24 ns (240 photons), sufficient for a future single-chip device to perform fully integrated quantum optics experiments such as boson sampling[4,5] with high photon numbers. Other important quantum information processing proposals such as fast single-photon switching[46] and photonic cluster state generation[47] will also benefit significantly from a short T_1.

Our work demonstrates that a high-performance QD-based SPS can be realized in a scalable on-chip geometry, requiring orders of magnitude less excitation power and space than existing spontaneous four-wave mixing sources[6] and benefitting from on-demand operation and a much higher photon generation rate. As such, our on-chip source has the potential to be a major step forward in fully integrated chip devices for quantum photonics[18].

Methods

Methods, including statements of data availability and any associated accession codes and references, are available at https://doi.org/10.1038/s41565-018-0188-x.

Received: 12 May 2017; Accepted: 7 June 2018;
Published online: 16 July 2018

References

1. Aaronson, S. & Arkhipov, A. The computational complexity of linear optics. In *43rd Annual ACM Symposium on Theory of Computing, STOC '11* 333–342 (ACM Press, New York, 2011).
2. Tillmann, M. et al. Experimental boson sampling. *Nat. Photon.* **7**, 540–544 (2013).
3. Broome, M. A. et al. Photonic boson sampling in a tunable circuit. *Science* **339**, 794–798 (2013).
4. Wang, H. et al. High-efficiency multiphoton boson sampling. *Nat. Photon.* **11**, 361–365 (2017).
5. Loredo, J. C. et al. Boson sampling with single-photon Fock states from a bright solid-state source. *Phys. Rev. Lett.* **118**, 130503 (2017).
6. Silverstone, J. W. et al. On-chip quantum interference between silicon photon-pair sources. *Nat. Photon.* **8**, 104–108 (2014).
7. Laucht, A. et al. A waveguide-coupled on-chip single-photon source. *Phys. Rev. X* **2**, 11014 (2012).
8. Lund-Hansen, T. et al. Experimental realization of highly efficient broadband coupling of single quantum dots to a photonic crystal waveguide. *Phys. Rev. Lett.* **101**, 113903 (2008).
9. Makhonin, M. N. et al. Waveguide coupled resonance fluorescence from on-chip quantum emitter. *Nano. Lett.* **14**, 6997–7002 (2014).
10. Reithmaier, G. et al. On-chip generation, routing, and detection of resonance fluorescence. *Nano. Lett.* **15**, 5208–5213 (2015).
11. Hausmann, B. J. M. et al. Integrated diamond networks for quantum nanophotonics. *Nano. Lett.* **12**, 1578–1582 (2012).
12. Sipahigil, A. et al. An integrated diamond nanophotonics platform for quantum optical networks. *Science* **354**, 847–850 (2016).
13. Santori, C., Fattal, D., Vucković, J., Solomon, G. S. & Yamamoto, Y. Indistinguishable photons from a single-photon device. *Nature* **419**, 594–597 (2002).
14. He, Y.-M. et al. On-demand semiconductor single-photon source with near-unity indistinguishability. *Nat. Nanotech.* **8**, 213–217 (2013).
15. Somaschi, N. et al. Near-optimal single-photon sources in the solid state. *Nat. Photon.* **10**, 340–345 (2016).
16. Ding, X. et al. On-demand single photons with high extraction efficiency and near-unity indistinguishability from a resonantly driven quantum dot in a micropillar. *Phys. Rev. Lett.* **116**, 020401 (2016).
17. Wang, H. et al. Near transform-limited single photons from an efficient solid-state quantum emitter. *Phys. Rev. Lett.* **116**, 213601 (2016).
18. Dietrich, C. P., Fiore, A., Thompson, M. G., Kamp, M. & Höfling, S. GaAs integrated quantum photonics: Towards compact and multi-functional quantum photonic integrated circuits. *Laser & Photonics Rev.* **10**, 870–894 (2016).
19. Liu, J. et al. Single self-assembledÿInAs/GaAs quantum dots in photonic nanostructures: The role of nanofabrication. *Phys. Rev. Appl.* **9**, 064019 (2018).
20. Kalliakos, S. et al. Enhanced indistinguishability of in-plane single photons by resonance fluorescence on an integrated quantum dot. *Appl. Phys. Lett.* **109**, 151112 (2016).

21. Kiraz, A., Atatüre, M. & Imamoğlu, A. Quantum-dot single-photon sources: Prospects for applications in linear optics quantum-information processing. *Phys. Rev. A.* **69**, 032305 (2004).
22. Purcell, E. Spontaneous emission probabilities at radio frequencies. *Phys. Rev.* **69**, 681 (1946).
23. Englund, D. et al. Controlling the spontaneous emission rate of single quantum dots in a two-dimensional photonic crystal. *Phys. Rev. Lett.* **95**, 13904 (2005).
24. Ota, Y. et al. Enhanced photon emission and absorption of single quantum dot in resonance with two modes in photonic crystal nanocavity. *Appl. Phys. Lett.* **93**, 183114 (2008).
25. Kress, A. et al. Manipulation of the spontaneous emission dynamics of quantum dots in two-dimensional photonic crystals. *Phys. Rev. B* **71**, 241304 (2005).
26. Badolato, A. et al. Deterministic coupling of single quantum dots to single nanocavity modes. *Science* **308**, 1158–1161 (2005).
27. Happ, T. D. et al. Enhanced light emission of $In_xGa_{1-x}As$ quantum dots in a two-dimensional photonic-crystal defect microcavity. *Phys. Rev. B* **66**, 41303 (2002).
28. Kim, J.-H., Cai, T., Richardson, C. J. K., Leavitt, R. P. & Waks, E. Two-photon interference from a bright single-photon source at telecom wavelengths. *Optica* **3**, 577–584 (2016).
29. Laurent, S. et al. Indistinguishable single photons from a single-quantum dot in a two-dimensional photonic crystal cavity. *Appl. Phys. Lett.* **87**, 163107 (2005).
30. Bentham, C. et al. On-chip electrically controlled routing of photons from a single quantum dot. *Appl. Phys. Lett.* **106**, 221101 (2015).
31. Coles, R. J. et al. Waveguide-coupled photonic crystal cavity for quantum dot spin readout. *Opt. Express* **22**, 2376–2385 (2014).
32. Reithmaier, G. et al. A carrier relaxation bottleneck probed in single InGaAs quantum dots using integrated superconducting single photon detectors. *Appl. Phys. Lett.* **105**, 081107 (2014).
33. Zibik, E. A. et al. Long lifetimes of quantum-dot inter-sublevel transitions in the terahertz range. *Nat. Mater.* **8**, 803–807 (2009).
34. Berstermann, T. et al. Systematic study of carrier correlations in the electron–hole recombination dynamics of quantum dots. *Phys. Rev. B* **76**, 165318 (2007).
35. Ramsay, A. J. et al. Phonon-induced Rabi-frequency renormalization of optically driven single InGaAs/GaAs quantum dots. *Phys. Rev. Lett.* **105**, 177402 (2010).
36. Melloni, A. et al. Tunable delay lines in silicon photonics: Coupled resonators and photonic crystals, a comparison. *IEEE Photonics J.* **2**, 181–194 (2010).
37. Matthiesen, C., Vamivakas, A. N. & Atatüre, M. Sub-natural linewidth single photons from a quantum dot. *Phys. Rev. Lett.* **108**, 093602 (2012).
38. Proux, R. et al. Measuring the photon coalescence time window in the continuous-wave regime for resonantly driven semiconductor quantum dots. *Phys. Rev. Lett.* **114**, 067401 (2015).
39. Bennett, A. J. et al. Cavity-enhanced coherent light scattering from a quantum dot. *Sci. Adv.* **2**, e1501256 (2016).
40. Iles-Smith, J., McCutcheon, D. P. S., Nazir, A. & Mørk, J. Phonon scattering inhibits simultaneous near-unity efficiency and indistinguishability in semiconductor single-photon sources. *Nat. Photon.* **11**, 521–526 (2017).
41. Thoma, A. et al. Exploring dephasing of a solid-state quantum emitter via time- and temperature-dependent Hong–Ou–Mandel experiments. *Phys. Rev. Lett.* **116**, 033601 (2016).
42. Wang, C. F. et al. Optical properties of single InAs quantum dots in close proximity to surfaces. *Appl. Phys. Lett.* **85**, 3423–3425 (2004).
43. Loredo, J. C. et al. Scalable performance in solid-state single-photon sources. *Optica* **3**, 433–440 (2016).
44. Löbl, M. C. et al. Narrow optical linewidths and spin pumping on charge-tunable close-to-surface self-assembled quantum dots in an ultrathin diode. *Phys. Rev. B* **96**, 165440 (2017).
45. Pernice, W. et al. High-speed and high-efficiency travelling wave single-photon detectors embedded in nanophotonic circuits. *Nat. Commun.* **3**, 1325 (2012).
46. Fan, S., Kocaba¸s, E. & Shen, J.-T. Input–output formalism for few-photon transport in one-dimensional nanophotonic waveguides coupled to a qubit. *Phys. Rev. A.* **82**, 063821 (2010).
47. Lindner, N. H. & Rudolph, T. Proposal for pulsed on-demand sources of photonic cluster state strings. *Phys. Rev. Lett.* **103**, 113602 (2009).

Acknowledgements

This work was funded by the EPSRC (UK) Programme Grants EP/J007544/1 and EP/N031776/1. The authors thank A. Ul-Haq, J. Iles-Smith, G. Buonaiuto, R. Kirkwood and S. Hughes for helpful discussions.

Author contributions

F.L. and A.J.B. designed and oversaw the experimental program. A.J.B., L.M.P.P.M. and F.L. developed the DPRF technique and carried out the measurements. J.O'H., L.M.P.P.M., A.J.B. and F.L. performed the SPAD lifetime measurements. J.O'H. and A.J.B. performed the RRS measurements with additional input from N.P.. A.J.B., J.O'H., L.M.P.P.M., F.L. and C.L.P. performed the pulsed correlation measurements. J.O'H. performed the master equation simulations of the system. R.J.C. designed and simulated the photonic structures. C.B. and I.E.I. performed initial characterization of the sample. E.C. grew the quantum dot wafer whilst B.R. fabricated the photonic nanostructures and processed the QD wafer into diodes with assistance from C.B.. L.R.W, I.E.I., M.S.S and A.M.F. provided supervision and expertise. F.L., A.J.B., J.O'H. and A.M.F. wrote the manuscript with input from all authors.

Competing interests

The authors declare no competing interests.

Additional information

Supplementary information is available for this paper at https://doi.org/10.1038/s41565-018-0188-x.

Reprints and permissions information is available at www.nature.com/reprints.

Correspondence and requests for materials should be addressed to A.J.B.

Publisher's note: Springer Nature remains neutral with regard to jurisdictional claims in published maps and institutional affiliations.

Methods

DPRF set-up. The QD is resonantly driven by a pair of variable duration pulses derived by splitting and Fourier-transform-shaping a broad 100 fs laser pulse generated from a Ti:Sapphire (Ti:S) laser with repetition rate 76.2 MHz. The Gaussian pulse width may be varied by adjusting the width of a slit placed slightly defocused from the Fourier plane. For most experiments, a duration of 13 ps is chosen to maximize the unfiltered signal-to-background ratio (by reduced spectral width) whilst remaining shorter than the QD radiative lifetime.

A cross-polarization configuration is adopted to detect the resonant QD emission (see details in Supplementary Information Section 8). The polarization direction of the laser pulses is initially defined by a Glan–Taylor prism, rotated by a $\lambda/2$ plate and reflected by a non-polarizing beam splitter. The combination of the $\lambda/2$ plate and the beam splitter allows us to easily set the polarization of the laser pulse. For these measurements, the laser pulses are 45° polarized with respect to the M1 cavity mode. The reflected laser is filtered out by a cross-polarizer. The distortion of the polarization of the laser by all optical components in both the excitation and detection paths is corrected by a $\lambda/4$ plate and an additional tunable waveplate with quarter-wave phase retardation.

The spectrally integrated signal to background ratio under π-pulse excitation (averaged laser power ~5 nW, see Supplementary Information Section 9) is ~20:1, smaller than that (~150:1) under CW excitation (laser power = 25 nW, see Supplementary Information Section 5C) due to difficulties in rejecting a broadband laser pulse using polarization. To fully separate the RF signal from the laser background in the DPRF measurement, the bias of the diode is modulated at a frequency of 11 Hz to move the QD in and out of resonance with the laser pulse. The laser background can be fully removed by subtracting the two spectra from each other (see example QD and background spectra in Fig. 1b).

SPAD lifetime measurements. The single-photon avalanche diode (SPAD) lifetime measurements are performed using the optical set-up of Supplementary Fig. 11 but using only a single excitation pulse. For the ensemble lifetime of QDs outside the photonic crystal, the excitation is provided by the unshaped (~100 fs) output of the Ti:S laser operating at $\lambda = 780$ nm. A 900 nm long-pass filter is inserted after the detection polarizer to remove the laser and any wetting layer emission from the detection path. The collection fibre is connected directly to a SPAD operating in Geiger mode with a Gaussian IRF of FWHM 350 ps. A time-correlated single-photon counting module (TCSPCM) synchronized with the laser pulse train records the arrival times of individual photons to produce the decay curves. For the QD-cavity lifetime measurements the zero-phonon line is filtered through the spectrometer (94 μeV bandwidth) before passing to a different SPAD with higher time resolution (IRF ~ 60 ps with a weak, longer tail) and being analysed by the TCSPCM as before. For the above-band lifetime measurement the excitation pulse is supplied by the unshaped laser at $\lambda = 802$ nm whilst the resonant π-pulse is provided by a single pulse-shaper as in the DPRF measurement but with the second pulse blocked.

Resonant Rayleigh scattering. For the RRS measurements a narrow-linewidth (<50 kHz) continuous-wave tunable Ti:S laser provides the excitation source. After the laser, the optical set-up is as in Supplementary Fig. 11 except that the emission is passed to the exit slit of the spectrometer and filtered as previously described. The emission then passes through a scanning Fabry–Pérot interferometer (FPI) and is detected with a SPAD. The FPI is swept by a function generator which also provides a synchronization signal to the TCSPCM, allowing conversion from SPAD detection time to spectral position. The excitation power is converted to Ω_R by measuring the power-dependent splitting of the Mollow triplet (see Supplementary Information Section 5B).

Correlation measurements. To perform the correlation measurements, the optical set-up described in Supplementary Fig. 11 is used. For measurements with the 13 ps pulse, the detection fibre is connected directly (bypassing the spectrometer) to a fibre Mach–Zehnder interferometer. One arm of the interferometer incorporates a $\lambda/2$ wave-plate and the other an additional length of fibre corresponding to a delay of T_{HOM}. Further details of the interferometer are contained within Supplementary Information Section 6. The two output ports of the interferometer are connected to a pair of single-photon avalanche photodiodes (combined Gaussian IRF has a FWHM 860 ps), which in turn are fed to the TCSPCM in order to measure the number of coincidence counts. For the 2.4 ps pulse, the spectrometer provides the additional filtering of the emission (96 μeV FWHM with Gaussian profile) and a pair of single-photon avalanche photodiodes with faster timing response are used (combined Gaussian IRF with 341 ps FWHM).

For HBT measurements, a single π-pulse per laser cycle (13.2 ns) is applied to the sample (the second pulse is blocked) and only the second fibre splitter of the interferometer is used. For HOM measurements, the full interferometer is used and a pair of π-pulses is applied to the sample as in the DPRF experiment. The pulse separation is matched to the interferometer delay by connecting the two pulses directly to the interferometer, scanning the delay line and observing the maxima of the classical interference between the two pulses.

Data availability. The data that support the plots within this paper and other findings of this study are available from https://doi.org/10.15131/shef.data.6241694.